Electronic States of Quinones for Organic Energy Devices: The Effect of Molecular Structure on Electrochemical Characteristics

Naoka Nagamura,[†,‡,§,⊥] Ryosuke Taniki,[‡,∇,⊥] Yuta Kitada,[‡] Asuna Masuda,[‡] Hiroaki Kobayashi,[‡] Nobuto Oka,[∥] and Itaru Honma*,[‡]

[†]National Institute for Materials Science, 1-2-1 Sengen, Tsukuba, Ibaraki 305-0047, Japan
[‡]Institute of Multidisciplinary Research for Advanced Materials, Tohoku University, 2-1-1, Katahira, Aoba-ku, Sendai 980-8577, Japan
[§]Japan Science and Technology Agency, PRESTO, 4-1-8 Honcho, Kawaguchi, Saitama 332-0012, Japan
[∥]Faculty of Humanity-Oriented Science and Engineering, Kindai University, 11-6, Kayanomori, Iizuka, Fukuoka 820-8555, Japan

S *Supporting Information*

ABSTRACT: The molecular design of organic energy-storage devices relies on correlations between the electrochemical properties of organic materials and their molecular structures. Here we report a systematic study of the fundamental electronic states of the quinone family of redox-active materials. Poly(ethylene oxide) coatings, as elution inhibitors, facilitated the evaluation of the electrochemical properties of single quinone molecules. Moreover, we confirmed experimentally how LUMO energies and their corresponding redox potentials depend on molecular structure, including the number of aromatic rings, the positions of functional groups, and coordination structures; this was achieved by elemental and chemical-state-selective X-ray absorption spectroscopy, and DFT calculations. We introduce an energy diagram depicting a segmentalized reduction process; this diagram considers the intermediate states during redox reactions to discuss processes that dominate changes in electrochemical properties as molecular structures are altered. Our results and analysis strategy are widely applicable to the material design of future organic molecular-based devices.

KEYWORDS: *organic redox-active material, quinone, X-ray absorption spectroscopy, X-ray photoemission spectroscopy, DFT calculation, energy diagram*
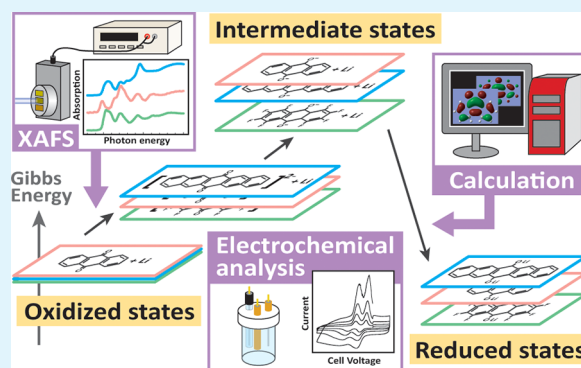
1. INTRODUCTION

Quinone-based organic molecules are attracting significant interest as redox-active materials for electrical energy storage systems due to several functional advantages, in addition to their cost effectiveness and low environmental burden. First, quinones undergo redox reactions that involve multiple π-conjugated electrons from carbonyl groups to afford high energy densities that are even equal to those of inorganic materials.[1,2] Second, quinone do not require tight crystal structures during their operation, unlike typical active inorganic materials,[3,4] because they undergo redox reactions in a single-molecular states when carrier cations are coordinated to their reduced forms in loose crystal structures that include intermolecular interactions.[1,2,5] This means that irreversible deterioration of the crystal structure does not need to be taken into account. Lastly, their electrochemical properties can be controlled through the molecular design of appropriate organic materials. These advantages have encouraged the use of quinones in a variety of applications,[6] such as redox flow batteries,[5,7] dual-electrolyte liquid batteries,[8] thin film solar cells,[9] and organic field effect transistors.[10]

However, the poor electron conduction and high solubility of quinones in electrolytes lead to limiting rate performance of these organic active materials.[11−13] Some approaches toward overcoming these problems have been reported; for example, the use of porous carbon as the supporting adsorbents for quinone molecules is one approach.[14−16]

Moreover, while electrochemical experiments reveal the redox chemistry of quinones in their initial and final states, the stabilities of the intermediate states, which are related to the activation energy in the redox reaction, need to be considered in order to evaluate the effectiveness of the process and to realize a functional molecular design for energy storage. The intermediate states in quinone redox chemistry have been discussed in previous theoretical studies using density functional theory (DFT);[17−19] however, there are mostly no experimental approaches in support of these calculations.

In this work, we report the successful evaluation of the redox reactions of quinones that accompany electronic and structural

changes through a combination study involving electrochemical experiments, DFT calculations, and spectroscopic analyses. Electrochemical experiments were carried out using poly-(ethylene oxide) (PEO) additives as elution inhibitor and activated carbon as the current collector. We used X-ray absorption spectroscopy (XAS) and X-ray photoemission spectroscopy (XPS) with elemental-selectivity and chemical-state-selectivity to reveal the electronic states of quinones that include their LUMO energies. DFT calculations strongly support the electrochemical and spectroscopic data and complement several electronic states during the redox reaction followed by drawing an energy diagram totally. A systematic study of the battery characteristics of the quinone family and the influence of molecular structure is presented below.

2. EXPERIMENTAL SECTION

All quinones were commercially available; their molecular structures are shown in Figure 1 and include 1,4-naphthoquinone (NQ),
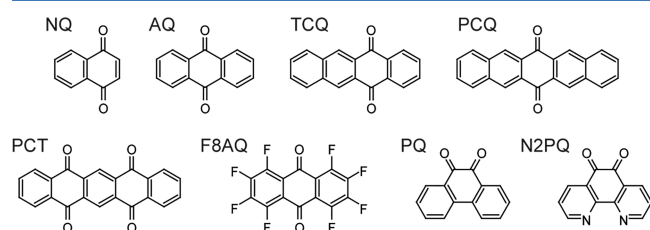

Figure 1. Molecular structures of NQ, AQ, TCQ, PCQ, PCT, F8AQ, PQ, and N2PQ.

anthraquinone (AQ), 5,12-tetracenequinone (TCQ), 6,13-pentacene-quinone (PCQ), 5,7,12,14-pentacenetetrone (PCT), octafluoro-9,10-anthraquinone (F8AQ), 9,10-phenanthrenequinone (PQ), and 1,10-phenanthroline-5,6-dione (N2PQ). The theoretical capacities of NQ, AQ, TCQ, PCQ, PCT, F8AQ, PQ, and N2PQ are 281.9, 257.5, 207.5, 173.8, 316.9, 152.2, 257.5, and 255.0 mA h g^{-1}, respectively. Quinone-supported activated carbon (AC) was mixed with poly(ethylene oxide) (PEO) and lithium bis(trifluoromethylsulfonyl)amide (LiTFSA) in water. Cathodes were prepared by mixing the obtained powder, acetylene black (AB), and poly(tetrafluoroethylene) (PTFE). The detail preparation process is described in the Supporting Information.

Battery tests were conducted using an HJ1001SD8 charge/discharge system (Hokuto Denko Corp.) at a scan rate of 0.2 C between 1.5 and 3.5 V at 35 °C. Reduced quinones were obtained electrochemically by reduction at a scan rate of 0.05 C to a lower cutoff potential of −2.0 V vs Ag$^+$/Ag in a three-electrode beaker cell. The reduced-quinone-dissolved electrolytes were dried under vacuum to remove solvents. Handling and analyses of the reduced quinones were carried out without exposure to air.

Nitrogen adsorption−desorption measurements were conducted using a BELSORP-18 single point surface area analyzer (MicrotracBEL Corp.), and the results were analyzed by the MP and t-plot methods. The concentration of NQ in the solvent was determined by UV−vis spectroscopy (UVN-6700, JASCO) with reference to a previously prepared standard curve. 1,4-Naphthoquinone was used to explore adsorption phenomena because an accurate standard curve for NQ had been prepared and it displays good solubility. The adsorption capacity of NQ on AC was calculated by subtracting the amount of NQ dissolved in acetone from the input value.

The X-ray photoelectron spectra ware acquired on a PHI 5000 Versa Prove 2TM spectrometer (ULVAC-PHI, INC.) using X-ray monochromators in combination with Al Kα radiation. C K-edge and O K-edge XAS spectra were acquired at the synchrotron soft X-ray beamline (BL-7A) at the Photon Factory, KEK. Pristine powder samples of purchased and reduced quinones were embedded in rubbed copper and indium foils to avoid charging effects. The surface-sensitive

total-electron-yield (TEY) mode was adopted, in which the sample current was measured as a function of incident X-ray energy.

Density functional theory (DFT) calculations were performed using Gaussian 09[20] at the wB97XD level of theory with the 6-311++G(d, p) basis set.[21−23] Overlap populations were extracted from the results of DFT calculation by the GaussSum software.[24]

3. RESULTS AND DISCUSSION

Figure 2A shows the micropore size distributions of AC, NQ supported on AC (AC-NQ), and NQ supported on AC with
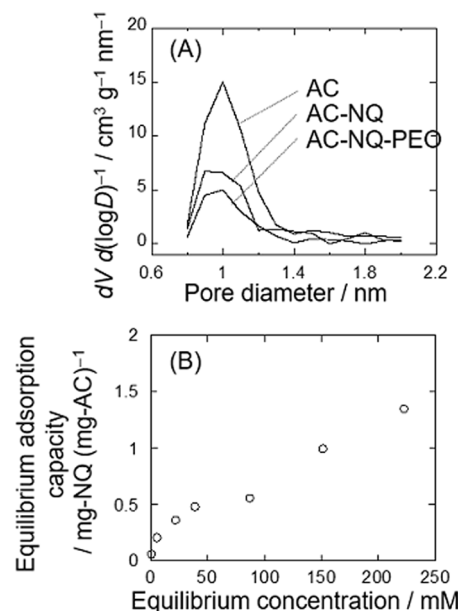

Figure 2. (A) Micropore distributions of AC, NQ-AC, and NQ-AC-PEO. (B) Adsorption isotherm of NQ to AC in acetone.

PEO (AC-NQ-PEO), which were determined by the MP method. The specific micropore surface areas of these samples obtained from t-plot analyses are 2932, 1474, and 910 m^2 (g of sample)$^{-1}$. The decreases in surface areas and differential volumes at pore diameters of around 1 nm indicate that these quinones are supported in the micropores.

Figure 2B shows the adsorption isotherm of NQ on AC (AC-NQ) in acetone. In the equilibrium concentration range (40−90 mM), the equilibrium adsorption capacity was observed to increase little, suggesting that the adsorption capacity of a single layer of NQ on AC is 0.5 mg of quinone/(mg of AC). Since the weight ratio of quinone to AC in the composite electrode used in this study is 30:70, we conclude that the quinone is thinly supported on the AC at the molecular level. The results of electrochemical studies using composite electrodes with different carbons (AB-NQ, AB-NQ-PEO, KB-NQ, KB-NQ-PEO, AC-NQ, and AC-NQ-PEO) are provided in the Supporting Information.

Figure 3A displays the second discharge curves at 0.2 C of the composite electrodes composed of NQ, AQ, TCQ, PCQ, or PCT supported by AC with PEO, which indicates the difference in electrochemical properties depending on the number of aromatic rings. The respective second discharge capacities of these composite electrodes are 203, 251, 190, 160, and 268 mA h g^{-1} after the electric double layer capacitance (EDLC) is subtracted from the raw data; these values are consistent with the respective theoretical capacities. Although quinones have little electronic conduction, they are supported with
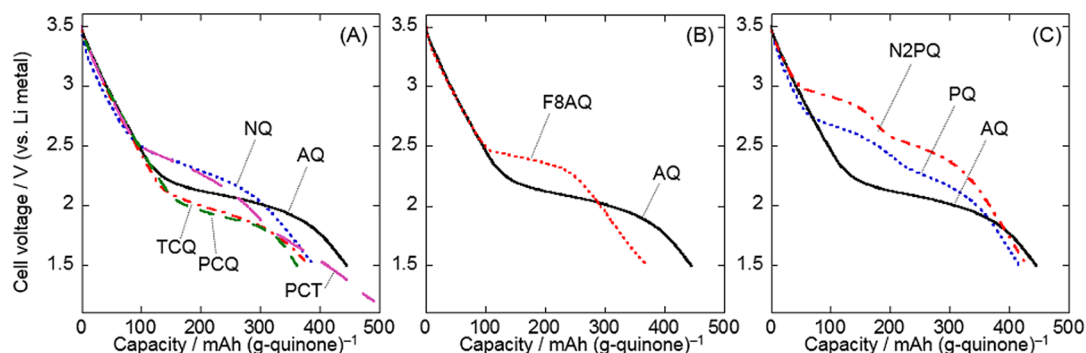
Figure 3. Second discharge curves of electrodes based on (A) NQ, AQ, TCQ, PCQ, and PCT; (B) AQ and F8AQ; (C) AQ, PQ, and N2PQ.

thinly enough to acquire electrons from the AC through redox processes. The redox voltage decreases with increasing number of aromatic rings in the following order: NQ > AQ > TCQ > PCQ. On the other hand, the charge–discharge curve for PCT exhibits two plateaus, at 2.4 and 1.7 V, which are closed to the respective plateaus of NQ and PCQ. This result for PCT suggests that the former redox reaction (2.4 V) involves an electronic state similar to that in NQ, while the latter (1.7 V) is similar to that of PCQ, which contains five hexagonal carbon rings just like PCT. Figure 3B displays the second discharge curves at 0.2 C of composite electrodes with AQ and F8AQ supported by AC with PEO, which indicates the difference in electrochemical properties between the presence and absence of functionals groups. The redox voltage of F8AQ is significantly higher than that of AQ. The effects of the number of aromatic rings and the presence of fluorine groups in these quinones on the redox potential are discussed in detail below. Figure 3C displays the second charge–discharge curves at 0.2 C of composite electrodes composed of AQ, PQ, and N2PQ supported by AC with PEO, which compares the effect of coordinating structures. Two clear plateaus appear in the curves of the PQ (2.7 and 2.3 V) and N2PQ (2.9 and 2.5 V) electrodes, and one plateau is evident in the curve of AQ (2.1 V). When two ketones are adjacent, as they are in PQ and N2PQ, radical anions formed from the neutral quinones through one electron reduction can exist stably by coordination to a bridging lithium ion. The coexistence of regions corresponding to neutral/quinone-radical anion and radical anion/divalent anion transitions gives rise to two plateaus in the charge–discharge curves of PQ and N2PQ. PQ exhibits higher redox voltages than AQ. Because the 1,2-dicarbonyl compound (PQ) experiences repulsion between the two dipolar ketones, the neutral quinone is destabilized relative to its 1,4-counterpart (lower LUMO energy, as described below) facilitating its reduction at a higher voltage than AQ. The heterocyclic analogue (N2PQ) has a higher redox voltage than PQ. From the perspective of complexation of chemistry, N2PQ behaves as a chelation ligand; one of the resonance forms of reduced N2PQ has a negatively charged nitrogen atom and lithium ions are possibly withdrawn not only at oxygen atoms but also at nitrogen atoms. This coordination ability of nitrogen atoms stabilizes the reduced form of N2PQ more than that of PQ, reflecting higher redox potentials as shown in Figure 3C. The cycling and rate performance of these catalysts are summarized in the Supporting Information.

In order to interpret the discharge curves and redox potentials of the structurally different quinones, we introduce a segmentalized energy diagram for the reduction process

involving several states, as shown in Figure 4 for AQ. During the first step (state 1 to 2), two electrons are transferred from
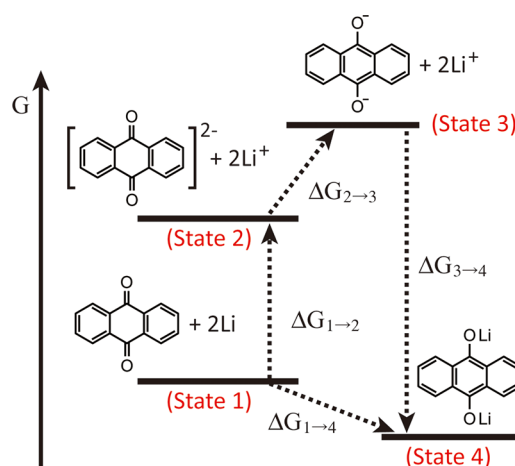

Figure 4. Energy diagram showing segmentalized reduction process for AQ involving several states.

Li metal to the LUMO of the quinones. This results in a higher overall system energy due to the large amount of destabilization associated with the formation of the Li cation, which is slightly offset by the small amount of stabilization resulting from the formation of the quinone anion (electron insertion to LUMO). Because antibonding molecular orbitals contribute to the LUMO of the quinone in its reduced form, the energy levels of orbitals drastically change accompanied by the redistribution of electrons in the molecular from the oxidized form to the reduced form after the insertion of the electrons into the LUMO of the initial state (state 2 to 3). State 2 is a resonance form owing to π orbitals in aromatic rings and conjugated structures. This electron delocalization stabilizes the system energy. So, the localized state, state 3, has higher energy than the delocalized state, state 2, as discussed later in Table 2. As a result of coordination to Li$^+$, the third step (state 3 to 4) results in reduced quinone of lower energy; and the energy gap between states 1 and 4 leads to the redox plateau observed in the discharge curves. The energy states are compared with reference to the quinone molecular structures through spectroscopy analyses and calculations, as discussed below.

In NEXAFS spectroscopy, the spectral features of specific elements reflect the partial densities of unoccupied states, as X-ray absorption processes involve transitions from core levels to multiple unoccupied states. In particular, the lowest energy peaks in the XAS spectra in thin study correspond to transitions
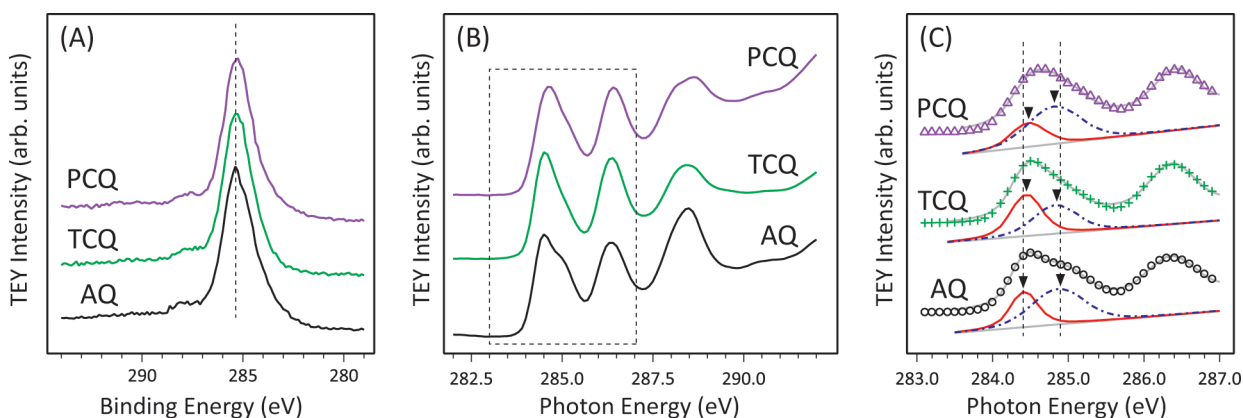
Figure 5. (A) C 1s XPS spectra and (B, C) C K-edge XAS spectra of AQ, TCQ, and PCQ on indium foils: (C) enlargement of panel B centered around 285 eV with two peaks fitted through deconvolution.

from a core level to the LUMO; consequently the energy of the LUMO can be confirmed experimentally. Since redox reactions essentially involve exchanges of electrons, the redox voltage is closely related to the LUMO energy in organic molecules, as reported previously.[25−27] The LUMO energy determined by XAS is associated with step 2 in Figure 4, namely, the insertion of an electron into the LUMO.

Figure 5 shows XPS and XAS spectra of AQ, TCQ, and PCQ. The C 1s XPS spectra of AQ, TCQ, and PCQ are similar. These molecules share a main peak at ∼285 eV. This result demonstrates that it is not necessary to take the core level shifts into account when interpreting the XAS spectra, which represent transitions from core levels to LUMO states. The lowest energy peak component at ∼284.4 eV in the C K-edge spectra (red solid curves in Figure 5C), corresponds to a transition from the C 1s state to the LUMO. The peak appears to shift to higher energies with increasing number of aromatic rings as indicated in Figure 5C.

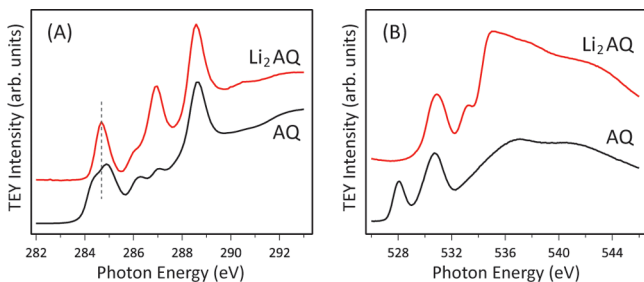The XAS spectra of the oxidized and reduced forms of AQ are presented in Figure 6. We transferred electrochemically

Figure 6. (A) C K-edge and (B) O K-edge XAS spectra of AQ on copper foils in oxidized and reduced forms.

reduced quinone samples using laminate cells and a transfer vessel to avoid air exposure. Clear differences are observed in both C K-edge and O K-edge spectra before and after the redox reaction. In the O K-edge spectra (Figure 6B), the peak at ∼528 eV is observed to disappear upon reducing, which indicates that a reaction center is an oxygen atom in a carbonyl group.

On the other hand, in the C K-edge spectra (Figure 6A), the two peaks at the absorption edge in the spectrum of AQ become one peak in the spectrum of Li_2AQ; the energy of this Li_2AQ peak (∼284.5 eV) does not coincide with the energies of

the peaks observed for AQ. To explain these electronic-state changes that accompany the redox reaction, the origins of the peaks need be correctly assigned.

Detailed peak assignments of the allowed unoccupied states in the C K-edge spectra are difficult to make using spectroscopic data; previous studies have only estimated spectroscopic results by comparing data with those of reference compounds.[28−31] Here we adopt overlap-population calculations to evaluate the energy levels of the unoccupied states and to associate them with the experimentally measured peak components. Molecular orbitals ($\Psi = \sum C_i \varphi_i$) were obtained by DFT calculations using GaussSum. The wB97XD level of theory was used to include the long-range interaction in our calculation.[21,22] The 6-311++G(d, p) diffuse function-augmented basis set[23] was adopted because we also calculated the energy states of quinone anions as discussed later. We have performed calculations simply in vacuum without solvent effects to compare with spectroscopic data.[12,32−34] The magnitude of the overlap population ($S_{ij} = C_i C_j \int \varphi_i^* \varphi_j \, d\tau$) at a particular energy level indicates the degree of contribution of the chemical bonds formed from the basis orbitals (φ_i and φ_j). Plus or minus overlap-population values indicate bonding or antibonding between two elements, i and j, respectively.

Figure 7A displays the energies of the unoccupied states near the LUMOs of AQ, TCQ, and PCQ, and the overlap populations of each of the unoccupied states derived from the calculations. The electron affinity is the free energy variation from a neutral system to a negatively charged system and indicates the energy level of the LUMO from the vacuum level. The unoccupied state with the largest absolute population value of electron affinity is assigned to be the LUMO. The energy level of the LUMO appears to approach the vacuum level with increasing numbers of hexagonal carbon rings in the quinone structures, leading to easier insertions of electrons into the quinone LUMOs. Using the LUMO energy of AQ as the reference, those of TCQ and PCQ are calculated to be +0.14 and +0.27 eV. This trend is consistent with the results obtained by XAS: +0.07 eV for TCQ and +0.18 eV for PCQ. Furthermore, transitions from the C 1s state to both C−C and C=O π* molecular orbitals are revealed to contribute to the formation of the LUMO by the overlap-population calculations. This result suggests that the intuitive one-to-one peak assignment is not always accurate. C−C and C−O overlap populations, with abundance ratios of 85:15 (AQ), 87:13 (TCQ), and 92:8 (PCQ), contribute to the LUMOs, indicating
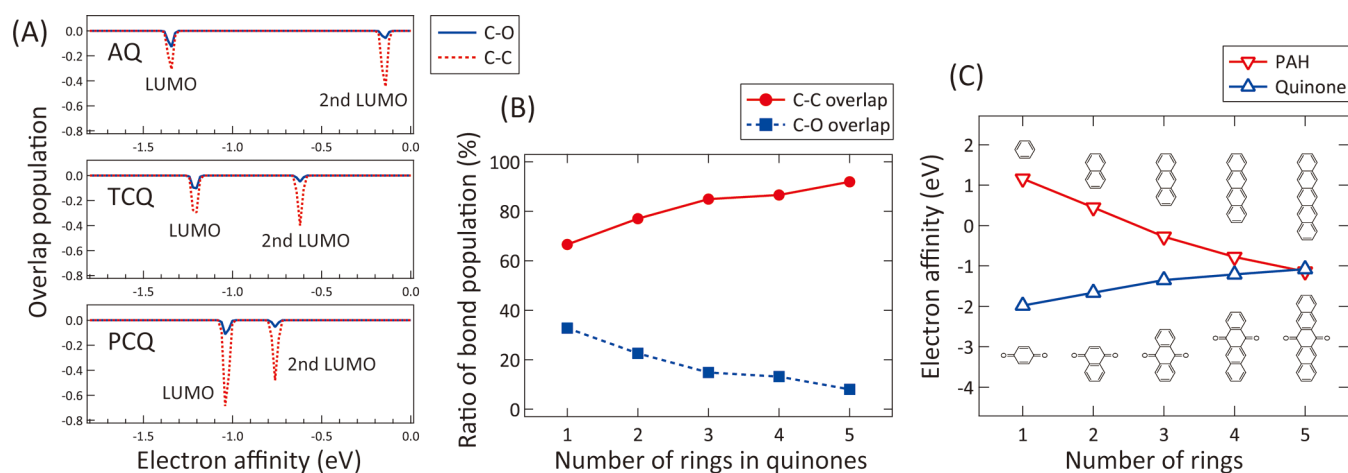
Figure 7. (A) Overlap populations of AQ, TCQ, and PCQ with electron affinity: energy levels of the LUMO from the vacuum level. (B) Overlap-population abundance ratios of five quinones based on C−C and C−O bonds at their LUMO levels. (C) Electron affinity of five quinones and five PAHs calculated at the wB97XD/6-311G++(d,p) level of theory using Gaussian 09.

that electrons are distributed to orbitals involving the C−C and C−O bonds in these ratios when electrons are inserted into the LUMO at the commencement of reduction.

The red solid curves at lower photon energy in Figure 5C correspond to C 1s C−C → LUMO state transition, while the blue dotted curves at higher photon energy correspond to C 1s C−C → second LUMO state transition. It is reasonable that C−C overlap populations in the LUMO and the second LUMO are larger than that of C−O in quinone molecules with several hexagonal carbon rings. Focusing on C−O bonding states, the ratios of the magnitude of C−O overlap populations in the LUMO to that in the second LUMO are 0.30:0.25 (AQ), 0.30:0.16 (TCQ), 0.35:0.20 (PCQ). In any case, C−O overlap populations in the LUMO are larger than those of the second LUMO. This suggests that the red solid curves in Figure 5C are "relatively" associated with C 1s C−C → C=O π* transition, while the blue dotted curves with C 1s C−C → C−C π* transition. Two peaks are clearly distinguished for AQ, but the peaks are not clearly separated for PCQ. This suggests that the energy difference between the two peaks decreases as the number of aromatic rings increases, which is in good agreement with the calculated results shown in Figure 7A.

Returning to Figure 6A, the lowest energy peak observed for AQ, which is now assigned to the C 1s C−C → C=O π* transition, is absent in the spectrum of Li₂AQ. We consider this to be caused by electron insertion into the LUMO by the introduction of Li;[35] the change in spectral shape at the O K-edge in Figure 6B is also due to this electron insertion. The peak assigned to the C 1s C−C → C−C π* transition seems to shift toward lower energy during the conversion of AQ into Li₂AQ. This suggests that not only are the C=O bonds in the carbonyl groups involved but also the delocalized electrons in the aromatic rings and conjugated structures are directly affected by the introduction of Li during the reduction process.

Figure 7B shows the overlap-population abundance ratios based on the C−C and C−O bonds in the LUMO as functions of the number of aromatic rings in the quinone structure. The C−O overlap-population ratio decreases as the number of hexagonal carbon rings increases. with increasing numbers of hexagonal rings. The effect of the carbonyl group on the LUMO was evaluated by comparing quinones with the corresponding polycyclic aromatic hydrocarbons (PAHs). Table 1 summarizes the DFT-calculated HOMO and LUMO

Table 1. HOMO and LUMO Energies of Quinones and Polycyclic Aromatic Hydrocarbons

	quinones		PAHs	
no. of hexagonal carbon rings	HOMO (eV)	LUMO (eV)	HOMO (eV)	LUMO (eV)
1	−9.93	−1.98	−9.08	1.16
2	−9.75	−1.66	−8.02	0.447
3	−9.56	−1.35	−7.35	−0.276
4	−8.49	−1.21	−6.89	−0.778
5	−8.42	−1.08	−6.57	−1.14

energies of five quinones and five PAHs. The HOMO energies of the quinones and PAHs shift to higher binding energies with increasing numbers of hexagonal carbon rings. Figure 7C shows the LUMO energies of the five quinones and five PAHs listed in Table 1 as functions of the number of hexagonal carbon rings. The LUMO energies of the PAHs gradually decrease with increasing numbers of hexagonal carbon rings, which is ascribable to the smaller PAHs having fewer resonance structures available; consequently, π electrons are less delocalized over their aromatic rings. On the other hand, the LUMO energies of the quinones gradually increase with increasing numbers of hexagonal carbon rings. This is because the C−O bonds have a large effect on the LUMO. In the quinones, the effect of the C−O bond increases with decreasing numbers of rings as shown in Figure 7B. The LUMO energy shifts observed for the quinones are a consequence of the C−O bond effect dominating over the resonance effect.

The total electronic energies in states 1, 3, and 4 (Figure 4) were obtained by summing the DFT-calculated electronic and zero-point energies of each species. Although there should be the effects of various lithium salts and salt decomposition products,[19,25] quinone anions and Li cations were calculated individually assuming that quinone anions and desorbed Li cations are well-separated for simplicity.[12,27,36,37] The total electronic energy of state 2 was obtained by adding the LUMO energy of the ground-state quinone (discussed above) and the ionization energy of lithium. The energy gap between states 2 and 3 ($\Delta G_{2\to3}$) was obtained by subtracting $\Delta G_{1\to2}$ from $\Delta G_{1\to3}$. Moreover, $\Delta G_{1\to2}$, $\Delta G_{2\to3}$, and $\Delta G_{3\to4}$ relative to the reference quinone (AQ), namely, $\Delta G'_{1\to2}$, $\Delta G'_{2\to3}$, and $\Delta G'_{3\to4}$, were obtained by subtraction:

**Table 2. Gibbs Free Energies (G_1, G_2, G_3, and G_4), Energy Gaps ($\Delta G_{1\to2}$, $\Delta G_{2\to3}$, and $\Delta G_{3\to4}$), and Energy Gap Differences Relative to AQ ($\Delta G'_{1\to2}$, $\Delta G'_{2\to3}$, $\Delta G'_{3\to4}$, and $\Delta G'_{1\to4}$) for AQ, TCQ, PCQ, F8AQ, PQ, and N2PQ**

	G_1	$\Delta G_{1\to2}$, $\Delta G'_{1\to2}$	G_2	$\Delta G_{2\to3}$, $\Delta G'_{2\to3}$	G_3	$\Delta G_{3\to4}$, $\Delta G'_{3\to4}$	G_4 ($\Delta G_{1\to4}$)	$\Delta G'_{1\to4}$
AQ	0	8.02, 0.00	8.05	3.66, 0.00	11.68	−15.69, 0.00	−4.01	0.00
TCQ	0	8.29, 0.27	8.29	3.25, −0.42	11.54	−15.54, 0.15	−4.00	0.01
PCQ	0	8.56, 0.54	8.56	2.88, −0.78	11.44	−15.18, 0.51	−3.74	0.27
F8AQ	0	5.20, −2.82	5.20	−2.16, −5.83	3.03	−15.68, 0.01	−12.65	−8.64
PQ	0	7.66, −0.36	7.66	3.86, 0.19	11.52	−17.65, −1.96	−6.13	−2.12
N2PQ	0	7.10, −0.92	7.10	3.99, 0.33	11.09	−17.28, −1.59	−6.19	−2.18

$$\Delta G'_{1\to2}(\text{TCQ}) = \Delta G_{1\to2}(\text{TCQ}) - \Delta G_{1\to2}(\text{AQ})$$

These standardized differences in Gibbs energies ($\Delta G'$) can be treated as differences in LUMO energies, differences in charge-redistribution energies, coordination energies, and redox potentials between AQ and the other quinones. Table 2 summarizes the total electronic Gibbs energies (G), the energy gaps (ΔG), and the standardized energy gaps ($\Delta G'$) for AQ, TCQ, PCQ, F8AQ, PQ, and N2PQ.

Figure 8 displays the energy diagrams for AQ, TCQ, and PCQ. Because the LUMO energy of TCQ is lower than that of
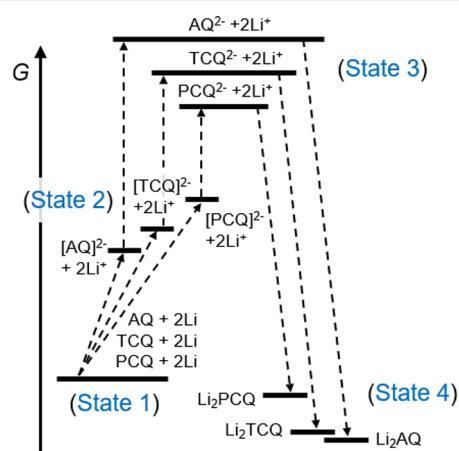

Figure 8. Energy diagram showing segmentalized reduction processes involving several states: AQ, TCQ, and PCQ.

AQ, as shown in Figure 5C and Figure 7A,C, the state of intermediate energy (state 2) of TCQ is higher than that of AQ by 0.27 eV following the insertion of two electrons into their LUMOs. The destabilization caused by charge redistribution raises the energy level to that of state 3, in which the energy gap of TCQ is lower than that of AQ by 0.42 eV. This difference is the result of AQ undergoing larger aromaticity changes than TCQ. The stabilization caused by Li coordination lowers the energy level to that of state 4 (the final state) where the energy change of AQ is larger than that of TCQ by 0.15 eV, which is due to the difference in the sizes of the quinone anions. The total energy gap of AQ ($\Delta G_{1\to4} = -4.01$ eV) is lower by 0.01 eV than that of TCQ ($\Delta G_{1\to4} = -4.00$ eV). Since smaller quinones are influenced more by their carbonyl groups, the charge redistributions resulting from changes in electronic states are affected significantly. The trend observed for PCQ is the same as that observed for TCQ, but the magnitude of the energy change is larger.

So far we have considered the relationship between the electronic states and electrochemical characteristics, and the number of aromatic rings in the quinone molecular structure.

Here we evaluate the effect of functional groups and coordinated quinone structures using the same strategy.

Figure 9 shows XPS and XAS spectra of AQ, F8AQ, and PQ. In the C 1s core-level spectrum of F8AQ, a peak component
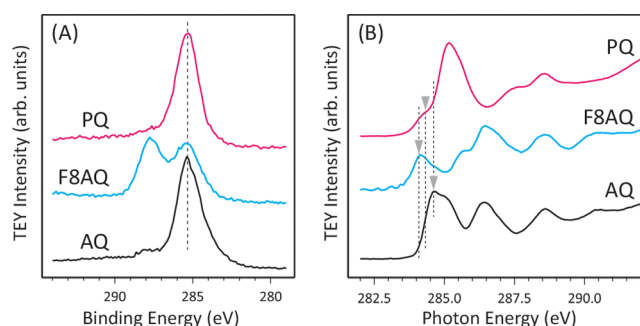
Figure 9. (A) C 1s XPS spectra and (B) C K-edge XAS spectra of AQ, F8AQ, and PQ on indium foils in their oxidized forms.

derived from C−F bonding is evident at ∼287 eV in addition to the C−C peak at ∼285 eV that corresponds to the main peak in the C 1s spectrum of AQ. The XAS spectra (Figure 9B) reveal that the lowest energy peak observed for F8AQ near the C K-edge is lower by 0.39 eV than that observed for AQ. Because the binding energy of the C−C component is deeper than that of the C−F component, the lowest energy peak in the XAS spectra at the C K-edge is assigned mainly to the C 1s C−C → C=O π^* transition, not the C 1s C−F → C=O π^* transition. Therefore, the lower LUMO peak observed for F8AQ ascribable to stabilization of the LUMO resulting from the introduction electron-withdrawing groups. The C−C peaks in the C 1s XPS spectra of AQ and PQ are similar, and the lowest energy peak in the XAS C K-edge spectrum of PQ is lower by 0.5 eV compared to that of AQ, which also indicates that the LUMO of PQ is stabilized by changing the relative positions of hexagonal carbon rings.

The LUMO energies of AQ, F8AQ, and PQ obtained by DFT calculations are −1.35, − 2.76, and −1.53 V, respectively. Figure 10 shows the calculated overlap populations of F8AQ and PQ relative to the vacuum level in the same way as that displayed in Figure 7A. Three overlap populations of the unoccupied states derived from C−O, C−C, and C−F contributions appear at the F8AQ LUMO level. The effect of fluorine substitution on the LUMO is identified. The LUMO level of F8AQ is lower than that of AQ because the aromatic fluorine substituents in F8AQ offer electrons through π bonding that stabilize the LUMO electronic state. On the other hand, the existence of a C−F antibonding overlap population of at the LUMO level of F8AQ risks decomposing the quinone. In fact, F8AQ begins to undergo electrochemically reductive decomposition at 1.6 V, as is evidenced by the discharge curve as shown in Figure 3B. If a fraction of electrons
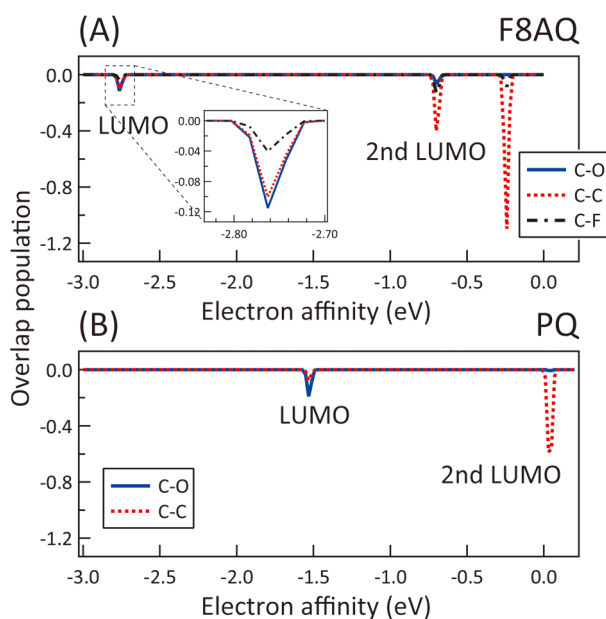
Figure 10. (A) F8AQ and (B) PQ overlap populations for energy levels between the LUMO and the vacuum level.

inserts into the antibonding C−F orbital at the LUMO level during reduction, breakage of the C−F bonds of the quinone becomes possible. As presented in Figure 10B, the overlap population at the LUMO level of PQ is mostly composed of contributions from C−O bonds. The large influence of the C−O bond on the LUMO lowers its energy, as described above.

Figure 11A displays the energy diagrams of the segmentalized reduction processes for AQ and F8AQ involving several
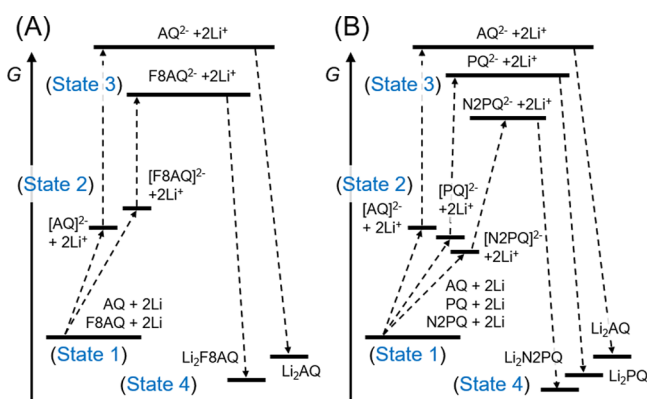

Figure 11. Energy diagram showing segmentalized reduction processes involving several states: (A) AQ and F8AQ; (B) AQ, PQ, and N2PQ.

states. The difference between AQ and F8AQ largely involves electron insertion into the LUMO, as found in state 2. No distinct differences are observed for the charge redistribution (state 2 → 3) and Li coordination (state 3 → 4) processes because the main backbones of both quinones are similar. The lowering of the LUMO energy through the addition of the fluorine atoms is the main factor that raises the redox potential. Figure 11B shows the similar energy diagrams for AQ, PQ, and N2PQ. The energy gap for PQ during the charge-redistribution process (state 2 → 3) is similar to that observed for AQ. This is because PQ and AQ have the same number of aromatic rings and the aromaticity of PQ is similar to that of AQ. However,

the difference between AQ and PQ is largely due to the Li coordination process (state 3 → 4). The two Li^+ cations in Li_2PQ are coordinated tetrahedrally between two oxygen atoms in adjacent carboxyl groups, whereas each Li^+ cation in Li_2PQ is coordinated linearly to an oxygen atom from each carboxyl group. The significant coordination within Li_2PQ leads to a large electrostatic interaction between the two Li^+ cations and the reduced quinone, followed by a lowering $\Delta G_{3\rightarrow4}$ that results in an increase in the redox potential. The total electronic energy of N2PQ is lowest because of two factors: its low LUMO energy and high coordination ability.

4. CONCLUSION

Simple quinones, AC, and a polymer were fabricated into composite electrodes. The degradation of battery performance derived from the dissolution of quinones into the electrolyte was partly restricted by polymer enwrapment, after which the quinones were successfully tested in electrochemical experiments. The influence of the quinone structure on the redox potential was investigated by electrochemical measurements, spectroscopy, and DFT calculations on the basis of a model in which the reduction was segmentalized into three processes: electron insertion into LUMO, charge redistribution, and Li^+ coordination. The electron-insertion process is influenced more by small quinones containing larger proportions of carboxyl groups, halogen-substituted quinones, and heterocyclic quinones. The charge-redistribution process is influenced by changes in aromaticity. The Li^+-coordination process is influenced by the size of the quinone and its coordination structure. Redox potentials are raised by low electron affinity, low levels of redistribution, and large Li^+-coordinating effects. We reveal the molecular-structure dependence of the electrochemical characteristics of these materials from the perspective of their electronic states and provide suggestions for quinone molecular design for better redox-active materials.

■ ASSOCIATED CONTENT

⑤ Supporting Information
The Supporting Information is available free of charge on the ACS Publications website at DOI: 10.1021/acsaem.7b00156.

　　Details of sample preparation procedures and electrochemical data (PDF)

■ AUTHOR INFORMATION

Corresponding Author
*E-mail: itaru.homma.e8@tohoku.ac.jp.

ORCID ⬤
Naoka Nagamura: 0000-0002-7697-8983

Present Address
▽TDK Corp., 570−2, Matsugashita, Minamihatori, Narita, Chiba, 286-8588, Japan.

Author Contributions
⊥N.N. and R.T. contributed equally to this work.

Notes
The authors declare no competing financial interest.

■ REFERENCES

(1) Liang, Y.; Tao, Z.; Chen, J. Organic Electrode Materials for Rechargeable Lithium Batteries. *Adv. Energy Mater.* **2012**, *2*, 742−769.

(2) Häupler, B.; Wild, A.; Schubert, U. S. Carbonyls: Powerful Organic Materials for Secondary Batteries. *Adv. Energy Mater.* **2015**, *5*, 1402034.

(3) Tarascon, J.-M.; Armand, M. Issues and Challenges Facing Rechargeable Lithium Batteries. *Nature* **2001**, *414*, 359−367.

(4) Ohzuku, T.; Ueda, A. Solid-State Redox Reactions of $LiCoO_2$ ($R\bar{3}m$) for 4 Volt Secondary Lithium Cells. *J. Electrochem. Soc.* **1994**, *141*, 2972−2977.

(5) Takeda, T.; Taniki, R.; Masuda, A.; Honma, I.; Akutagawa, T. Electron-deficient Anthraquinone Derivatives as Cathodic Material for Lithium Ion Batteries. *J. Power Sources* **2016**, *328*, 228−234.

(6) Son, E.; Kim, J.; Kim, K.; Park, C. Quinone and Its Derivatives for Energy Harvesting and Storage Materials. *J. Mater. Chem. A* **2016**, *4*, 11179−11202.

(7) Lin, K.; Chen, Q.; Gerhardt, M. R.; Tong, L.; Kim, S. B.; Eisenach, L.; Valle, A. W.; Hardee, D.; Gordon, R. G.; Aziz, M. J.; Marshak, M. P. Alkaline Quinone Flow Battery. *Science* **2015**, *349*, 1529−1532.

(8) Ding, Y.; Yu, G. A Bio-Inspired, Heavy-Metal-Free, Dual-Electrolyte Liquid Battery towards Sustainable Energy Storage. *Angew. Chem., Int. Ed.* **2016**, *55*, 4772−4776.

(9) Cheng, M.; Yang, X.; Zhang, F.; Zhao, J.; Sun, L. Efficient Dye-Sensitized Solar Cells Based on Hydroquinone /Benzoquinone as a Bioinspired Redox Couple. *Angew. Chem., Int. Ed.* **2012**, *51*, 9896−9899.

(10) Mamada, M.; Kumaki, D.; Nishida, J.; Tokito, S.; Yamashita, Y. Novel Semiconducting Quinone for Air-Stable n-Type Organic Field-Effect Transistors. *ACS Appl. Mater. Interfaces* **2010**, *2*, 1303−1307.

(11) Yao, M.; Senoh, H.; Sakai, T.; Kiyobayashi, T. 5,7,12,14-Pentacenetetrone as a High-Capacity Organic Positive-Electrode Material for Use in Rechargeable Lithium Batteries. *Int. J. Electrochem. Sci.* **2011**, *6*, 2905−2911.

(12) Yao, M.; Yamazaki, S.; Senoh, H.; Sakai, T.; Kiyobayashi, T. Crystalline Polycyclic Quinone Derivatives as Organic Positive-electrode Materials for Use in Rechargeable Lithium Batteries. *Mater. Sci. Eng., B* **2012**, *177*, 483−487.

(13) Nishida, S.; Yamamoto, Y.; Takui, T.; Morita, Y. Organic Rechargeable Batteries with Tailored Voltage and Cycle Performance. *ChemSusChem* **2013**, *6*, 794−797.

(14) Lei, Z.; Wei-kun, W.; An-bang, W.; Zhong-bao, Y.; Shi, C.; Yu-sheng, Y. A MC/AQ Parasitic Composite as Cathode Material for Lithium Battery. *J. Electrochem. Soc.* **2011**, *158*, A991−A996.

(15) Le Comte, A.; Chhin, D.; Gagnon, A.; Retoux, R.; Brousse, T.; Belanger, D. Spontaneous Grafting of 9,10-phenanthrenequinone on Porous Carbon as an Active Electrode Material in an Electrochemical Capacitor in an Alkaline Electrolyte. *J. Mater. Chem. A* **2015**, *3*, 6146−6156.

(16) Jaffe, A.; Saldivar Valdes, A.; Karunadasa, H. I. Quinone-Functionalized Carbon Black Cathodes for Lithium Batteries with High Power Densities. *Chem. Mater.* **2015**, *27*, 3568−3571.

(17) Er, S.; Suh, C.; Marshak, M. P.; Aspuru-Guzik, A. Computational Design of Molecules for an All-Quinone Redox Flow Battery. *Chem. Sci.* **2015**, *6*, 885−893.

(18) Wheeler, D. E.; Rodriguez, J. H.; McCusker, J. K. Density Functional Theory Analysis of Electronic Structure Variations across the Orthoquinone/Semiquinone/Catechol Redox Series. *J. Phys. Chem. A* **1999**, *103*, 4101−4112.

(19) Kim, K. C.; Liu, T.; Lee, S. W.; Jang, S. S. First-Principles Density Functional Theory Modeling of Li Binding: Thermodynamics and Redox Properties of Quinone Derivatives for Lithium-Ion Batteries. *J. Am. Chem. Soc.* **2016**, *138*, 2374−2382.

(20) Frisch, M. J.; Trucks, G. W.; Schlegel, H. B.; Scuseria, G. E.; Robb, M. A.; Cheeseman, J. R.; Scalmani, G.; Barone, V.; Mennucci, B.; Petersson, G. A.; et al. *Gaussian 09*, Revision D.01; Gaussian: Wallingford, CT, USA, 2013.

(21) Becke, A. D. Density-Functional Thermochemistry. III. The Role of Exact Exchange. *J. Chem. Phys.* **1993**, *98*, 5648−5652.

(22) Chai, J.-D.; Head-Gordon, M. Long-Range Corrected Hybrid Density Functionals with Damped Atom-Atom Dispersion Corrections. *Phys. Chem. Chem. Phys.* **2008**, *10*, 6615−6620.

(23) McLean, A. D.; Chandler, G. S. Contracted Gaussian Basis Sets for Molecular Calculations. I. Second Row Atoms, Z = 11−18. *J. Chem. Phys.* **1980**, *72*, 5639−5648.

(24) O'Boyle, N. M.; Tenderholt, A. L.; Langner, K. M. cclib: A Library for Package-Independent Computational Chemistry Algorithms. *J. Comput. Chem.* **2008**, *29*, 839−845.

(25) Bachman, J. E.; Curtiss, L. A.; Assary, R. S. Investigation of the Redox Chemistry of Anthraquinone Derivatives Using Density Functional Theory. *J. Phys. Chem. A* **2014**, *118*, 8852−8860.

(26) Djurovich, P. I.; Mayo, E. I.; Forrest, S. R.; Thompson, M. E. Measurement of the Lowest Unoccupied Molecular Orbital Energies of Molecular Organic Semiconductors. *Org. Electron.* **2009**, *10*, 515−520.

(27) Nokami, T.; Matsuo, T.; Inatomi, Y.; Hojo, N.; Tsukagoshi, T.; Yoshizawa, H.; Shimizu, A.; Kuramoto, K.; Komae, K.; Tsuyama, H.; Yoshida, J. Polymer-Bound Pyrene-4,5,9,10-tetraone for Fast-Charge and -Discharge Lithium-Ion Batteries with High Capacity. *J. Am. Chem. Soc.* **2012**, *134*, 19694−19700.

(28) Francis, J. T.; Hitchcock, A. P. Inner-Shell Spectroscopy of P-benzoquinone, Hydroquinone, and Phenol: Distinguishing Quinoid and Benzenoid Structures. *J. Phys. Chem.* **1992**, *96*, 6598−6610.

(29) Bässler, M.; Fink, R.; Buchberger, C.; Väterlein, P.; Jung, M.; Umbach, E. Near Edge X-ray Absorption Fine Structure Resonances of Quinoide Molecules. *Langmuir* **2000**, *16*, 6674−6681.

(30) Solomon, D.; Lehmann, J.; Kinyangi, J.; Liang, B.; Heymann, K.; Dathe, L.; Hanley, K.; Wirick, S.; Jacobsen, C. Carbon (1s) NEXAFS Spectroscopy of Biogeochemically Relevant Reference Organic Compounds. *Soil Sci. Soc. Am. J.* **2009**, *73*, 1817−1830.

(31) Heymann, K.; Lehmann, J.; Solomon, D.; Schmidt, M. W. I.; Regier, T. C 1s K-edge Near Edge X-ray Absorption Fine Structure (NEXAFS) Spectroscopy for Characterizing Functional Group Chemistry of Black Carbon. *Org. Geochem.* **2011**, *42*, 1055−1064.

(32) Kera, S.; Hosoumi, S.; Sato, K.; Fukagawa; Nagamatsu, S.; Sakamoto, Y.; Suzuki, T.; Huang, H.; Chen, W.; Wee, A. T. S.; Coropceanu, V.; Ueno, N. Experimental Reorganization Energies of Pentacene and Perfluoropentacene: Effects of Perfluorination. *J. Phys. Chem. C* **2013**, *117*, 22428−22437.

(33) Lima, I. T.; Sousa, L.; Freitas, R. d. S.; Ribeiro, L. A., Jr.; de Sousa, R. T., Jr.; da Silva Filho, D. A. A DFT Study of a Set of Natural Dyes for Organic Electronics. *J. Mol. Model.* **2017**, *23*, 343.

(34) Peng, Q.; Obolda, A.; Zhang, M.; Li, F. Organic Light-Emitting Diodes Using a Neutral π Radical as Emitter: The Emission from a Doublet. *Angew. Chem., Int. Ed.* **2015**, *54*, 7091−7095.

(35) Chen, C. T.; Tjeng, L. H.; Rudolf, P.; Meigs, G.; Rowe, J. E.; Chen, J.; McCauley, J. P., Jr; Smith, A. B., III; McGhie, A. R.; Romanow, W. J.; Plummer, E. W. Electronic States and Phases of

K$_x$C$_{60}$ from Photoemission and X-ray Absorption Spectroscopy. *Nature* **1991**, *352*, 603−605.

(36) Yokoji, T.; Matsubara, H.; Satoh, M. Rechargeable Organic Lithium-Ion Batteries using Electron-Deficient Benzoquinones as Positive Electrode Materials with High Discharge Voltages. *J. Mater. Chem. A* **2014**, *2*, 19347−19354.

(37) Yang, S.-J.; Qin, X.-Y.; He, R.; Shen, W.; Li, M.; Zhao, L.-B. A Density Functional Theory Study on the Thermodynamic and Dynamic Properties of Anthraquinone Analogue Cathode Materials for Rechargeable Lithium Ion Batteries. *Phys. Chem. Chem. Phys.* **2017**, *19*, 12480−12489.